# CFD-METHODS APPLIED TO DISPERSED PARTICLE FLOW WITHIN MELT POOLS DURING LASER INDUCED SURFACE MODIFICATION PROCESSES OF CERAMICS

**M. Rohde***

*Forschungszentrum Karlsruhe GmbH ,Institute of Materials Research I,
Hermann-von-helmholtz-Platz 1, 76344 Eggenstein, Germany
e-mail: magnus.rohde@imf.fzk.de
Web page: http://www.fzk.de/imf

**Key words:** Heat transfer, Mass transport, Multiphase flow, Phase transformation, Laser heating

**Abstract.** *Laser supported processes can be used to modify the electrical and thermal properties of ceramic substrates locally. These processes are characterised by a strong thermal interaction between the laser beam and the ceramic surface which leads to localised melting. During the dynamic melting process an additive material is injected into the melt pool in order to modify the physical properties. The heat and mass transfer during this dynamic melting and solidification process has been studied numerically in order to identify the dominating process parameters. Simulation tools based on a finite volume method have been developed to describe the heat transfer, fluid flow and the phase change during the melting and solidification of the ceramic. The results of the calculation have been validated against experimental results.*

## 1 INTRODUCTION

Laser supported surface dispersing and alloying of ceramics are important methods to modify the properties of this class of brittle and non-conducting materials. Using this laser process, mechanical and tribological properties[1] can be improved, thermal and electrical conductance can be adjusted[2,3.] Furthermore, the property modifications are restricted to a localised area leaving the bulk of the ceramic in its original state. However, due to the complex relationship between the process parameters and results of the laser alloying optimisation procedures are often time consuming and only guided by a long term experimental experience. Therefore, simulation tools with the ability to predict experimental results, or at least to restrict parameter fields, would be helpful to reduce the time of the process development.

Heat, fluid flow and mass transfer in laser assisted surface modification have been studied within a numerical approach by several researchers in the past[4-12]. All these models have been applied to the laser processing of metal alloy systems. Although the heat transfer and the solid-liquid phase change during the thermal processing of ceramic particles and metal-ceramic composites has been treated numerically by several authors[13, 14], the laser processing

of ceramics has been studied only in a relatively small number of studies[15, 16]. The objective of this paper is therefore to get more insight in the dominating thermal processes during the laser ceramic interaction and also to enlarge the available database for engineering applications.

In this paper we study the dynamic liquid-solid phase change and the distribution of the second phase within the melt pool generated during the process as a function of the process parameters in ceramic substrates. The temperature, the velocity profiles and the volume fraction of the metal particles have been calculated by the CFD-code PHOENICS[17], which uses the finite volume method to integrate the corresponding energy and Navier-Stokes equations, respectively. For the modelling of the liquid-solid phase change process an enthalpy-porosity technique is applied. Particularly, the laser induced dispersing of TiN particles into pure $Al_2O_3$ substrates and $Al_2O_3$ reinforced with $ZrO_2$ has been considered in this study within a comparison of two different process modes.

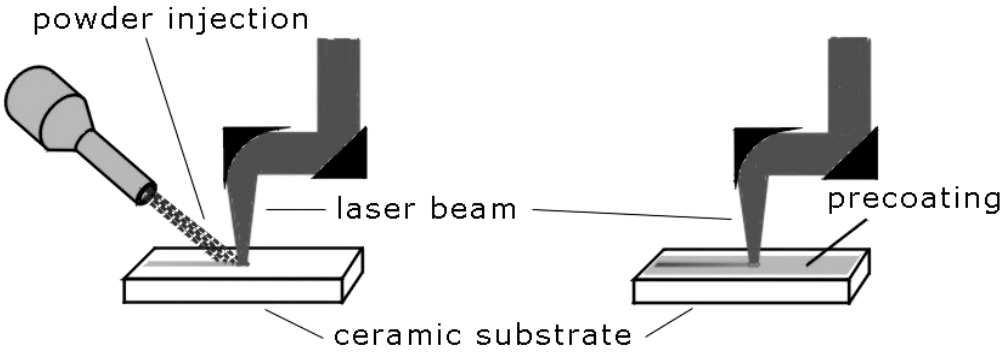


Figure 1: Schematics of the laser induced surface modification. One step process (left): particles are injected into the melt pool through a nozzle during the laser process. Two step process (right): A pre-placed powder coating of metallic particles is applied to the surface of the substrate prior to the laser process.

## 2 LASER PROCESS

The principle of the process is shown in fig. 1. The laser beam of a high power $CO_2$-laser is used to heat the surface of the ceramic above the melting point. Metallic particles are introduced into the localised melt pool. After the solidification a metal-ceramic composite has been generated within the laser irradiated trace. This can be achieved by using a one step process, which utilises the direct injection of the metal powder into the laser molten pool, or a two step process in which a pre-placed powder coating is incorporated into the surface of the ceramic during the laser induced remelting (see fig. 1). During the laser process the ceramic substrate is heated up to temperatures of 1500 °C in order to avoid thermally induced cracking. In order to generate modified regions the laser beam is moved across the surface of the substrate with a constant velocity. For the most experiments a $CO_2$-laser ($\lambda_{CO2} = 10.6$ µm)

with a maximum power of 500 W was used. The laser beam was shaped using a line optics giving a rectangular intensity distribution with a length of 1 mm and width of 6 mm. The laser power was varied between 200 - 400 W. The scanning velocity of the laser was typically adjusted between 125 and 1000 mm/min.

## 3 CERAMIC SUBSTRATE MATERIALS

Two different ceramic substrate materials have been considered within this study. An alumina substrate with a small porosity of 5 % and a zirconia reinforced alumina consisting of 10 wt.-% $ZrO_2$ and 90 wt.- % $Al_2O_3$. The relevant thermophysical parameters (see table 1) were measured as a function of temperature up to 1500 °C using standard measurement techniques[18]. The data for the density, thermal diffusivity and the coefficient of thermal expansion (CTE) in table I are given for the temperature of 1500 °C, i.e. the pre-heating temperature of the ceramics before and during the laser process. The thickness of the substrates was 8 mm, the length 50 mm and the width 18 mm.

| | **Al24 ($Al_2O_3$)** | **SN80 ($90Al_2O_3$-$10ZrO_2$)** | **TiN** |
|---|---|---|---|
| Porosity, % | 5 | - | - |
| Average particle size (□m) | - | - | 6 |
| Density, g/cm$^3$ | 3.32 | 3.90 | 5.16 |
| Thermal diffusivity, cm$^2$/s<br>at T=1500°C<br>at T= $T_M$ | <br>0.010<br>0.008 | <br>0.011<br>0.009 | <br>0.063 [32] |
| Heat capacity, J/gK<br>at T=1500°C<br>at T=$T_M$ | <br>1.45<br>1.52 | <br>1.44<br>1.51 | |
| $T_M$, °C | 2040 | 1890 | 3290 |
| CTE, $10^{-6}$ K$^{-1}$ at T=1500°C | 10.2 | 10.6 | 10.55 [32] |
| Latent heat, J/g | 1.07 $10^3$ [31] | 1.03 $10^3$ [31] | - |

Table 1: Material properties

## 4 NUMERICAL METHOD

The CFD-software PHOENICS[17] has been used to solve the Navier-Stokes equations which describes the fluid flow within the melt pool due to the surface tension gradient (Marangoni convection) which is induced by the localised heat source travelling with a constant speed. The heat source is generated by a focused laser beam with a strip-like intensity profile which superimposes a strong transient temperature gradient on the surface. Temperature dependent material properties like the thermal conductivity and the heat capacity has been included in the model. Since for alumina ceramics the thermal conductivity decreases with a approximately $T^{-1}$ behaviour[19], the variation of this property between 1400 °C and the melting point becomes relatively small. Within this temperature interval the heat

capacity also increases only slightly. Therefore, for both properties the variation between the pre-heating temperature of 1500 °C and the melting point was described by a linear function of the temperature. The calculated values are given in table I. Above the melting point a constant behaviour was assumed.

The computation has been performed under the assumption that the flow is laminar, the fluid is incompressible with a flat free surface and the Boussinesq approximation is valid for the temperature dependent density variation within the melt[20], which induces thermal buoyancy forces due to temperature gradients.

The governing equations, which describe the velocity (u,v) and temperature (T) distribution, for the numerical modelling of the process are:

continuity
$$\frac{\partial(\rho u)}{\partial x}+\frac{\partial(\rho v)}{\partial y}=0 \tag{1}$$

x-momentum
$$\frac{\partial u}{\partial t}+u\cdot\nabla u=\frac{1}{\rho}\frac{\partial P}{\partial x}+\mu\Delta u \tag{2}$$

y-momentum
$$\frac{\partial v}{\partial t}+v\cdot\nabla v=\frac{1}{\rho}\frac{\partial P}{\partial x}+\mu\Delta v-\beta g\cdot\left(T-T_M\right) \tag{3}$$

energy
$$\frac{\partial T}{\partial t}+u\cdot\frac{\partial T}{\partial x}+v\cdot\frac{\partial T}{\partial y}=\kappa\cdot\Delta T \tag{4}$$

with x,y and t are the spatial and time coordinates, respectively, P is the pressure, ρ the density, μ the viscosity, κ the thermal diffusivity, β the volumetric thermal expansion coefficient, g the gravitational force constant and $T_M$ the melting temperature.

The boundary conditions at the surface at y = 0 are

$$v=0 \tag{5}$$

$$\mu\cdot\frac{\partial v}{\partial y}=-\frac{\partial\sigma}{\partial T}\frac{\partial T}{\partial x} \tag{6}$$

$$Q_{Las}=\eta\cdot P_{Las}\cdot a_{Las}\left(v_{Scan},t\right)\cdot\left(\frac{1}{1+e^{-(x-x_0)/f}}+\frac{1}{1+e^{(x-x_0)/f}}+1\right) \tag{7}$$

with
$$a_{Las}(v_{Scan},t)=\frac{1}{1+e^{-(z-v_{Scan}\ t)/f}}+\frac{1}{1+e^{(z-(v_{Scan}t+d_{Las}))/f}}+1 \tag{7a}$$

The boundary conditions given by the equations (5) – (7) accounts for the fact that the y-component of the velocity field vanishes (eq. 5) at the free surface, shear forces are generated (eq. 6) at the surface of the melt pool due to a gradient in the surface tension σ and a time dependent heat flux $Q_{Las}$ through the liquid-gas boundary (eq. 7) is induced due to the absorption of the laser energy with a rectangular (6x1 mm) intensity profile. The first coefficients in eq. 7 are the absorption efficiency η and $P_{Las}$ the power density of the laser beam, respectively. The following term $a_{Las}$ accounts for the time dependent part of the heating profile, which gives a rectangular profile travelling with the scanning velocity $v_{Scan}$ of the laser beam in the z-direction. The last term of the equation describes the lateral variation of the profile. The coefficient f determines the sharpness of the profile and is set to a value of

$10^{-5}$ for the model calculations.

The transport of the alloying material due to convection and diffusion within the melt pool can be expressed by

$$\frac{\partial(\rho C_{Part})}{\partial t}+\frac{\partial(\rho u C_{Part})}{\partial x}+\frac{\partial(\rho v C_{Part})}{\partial y}=\frac{\partial}{\partial x}\left(D\frac{\partial C_{Part}}{\partial x}\right)+\frac{\partial}{\partial y}\left(D\frac{\partial C_{Part}}{\partial y}\right) \tag{8}$$

where $C_{Part}$ is the volume fraction of the particles and D the diffusivity.

The moving melting-solidification boundary and the liquid-solid phase change have been considered in the model by implementing the enthalpy-porosity method [21, 22] into PHOENICS. In order to achieve this implementation additional source terms has been introduced in the momentum (2), (3) and energy equations (4) which take into account that the velocity components vanish in the solid phase and that the enthalpy changes due to the latent heat during the melting process. The PHOENICS user interface "In-Form" [17], which allows for the transmission of mathematical expressions to the solver by input of formulas in the model description files, has been used to implement these terms. Using the "In-Form" formalism the model can be adapted to the requirements of the user by writing the mathematical expression into the PHOENICS input file. The additional linking of a user defined subroutine is therefore not necessary.

The enthalpy- and porosity function $F_{Liq}(T)$ and A(T), which were used for the simulations within this study, are given in equation 9 and 10, respectively.

$$F_{Liq}(T)=\frac{1}{1+e^{-(T-T_M)/\varepsilon}} \tag{9}$$

$$A(T)=\frac{C_N\cdot(1-F_{Liq})^2}{F_{Liq}{}^3+q}\quad ;\ q=0.001;C_N=1.5\cdot10^3 \tag{10}$$

The values of constants $C_N$ and q are chosen as results of test simulations. The functions given by the equations 9 and 10 have been introduced into the momentum- and energy-equation as additional source terms:

$$\frac{\partial \upsilon}{\partial t}+\upsilon\cdot\nabla\upsilon=-\frac{1}{\rho}\frac{\partial P}{\partial x}+\mu\Delta\upsilon-A\cdot(\upsilon-\upsilon_{Scan}) \tag{11}$$

$$\frac{\partial v}{\partial t}+v\cdot\nabla v=-\frac{1}{\rho}\frac{\partial P}{\partial y}+\mu\Delta v-\rho\beta g\cdot\left(T-T_M\right)-A\cdot(v-v_{Scan}) \tag{12}$$

$$\frac{\partial T}{\partial t}+\upsilon\cdot\frac{\partial T}{\partial x}+v\cdot\frac{\partial T}{\partial y}=\kappa\cdot\Delta T-L\cdot\left[\frac{\partial(\rho F_{Liq})}{\partial t}+\frac{\partial(\rho\upsilon F_{Liq})}{\partial x}+\frac{\partial(\rho v F_{Liq})}{\partial y}\right] \tag{13}$$

At temperatures above the melting temperature $T_M$ the porosity function A vanishes and F, which can be taken as a fraction of the liquid phase, equals one. Therefore, the additional source terms also reduces to zero, which leads the normal form of the Navier-Stokes equations given by eq. 2,3 and 4, since the continuity equations is not affected. At temperatures below $T_M$ the A increases to high values and consequently reduces the velocity components close to zero. Since the liquid fraction is also zero, the system of equation reduces to an expression for heat diffusion within a solid, since the convection terms are

suppressed. The second term of the RHS of eq. 13, which takes the evolution of the latent heat L at the melting or solidification front into account, contributes only non-zero values close to the melting point.

In order to consider the discrete nature of the powder particle flow and its interaction with the continuous molten phase an additional source term added to the momentum equations was used by the PHOENICS-solver [23]. The drag force is given by:

$$F_{Drag} = 0.5\, C_D\, \pi R_P^2\, \rho_{Fluid}\, (v_P - v_{Fluid})^2 \qquad (14)$$

with $R_P$ the radius of the particle, $v_P$ and $v_{Fluid}$ the velocity of the particle and the fluid, respectively

The drag coefficient $C_D$ for a spherical particle is approximately 0.5. The average particle size of the TiN-powder used in this study is given in table I.

For the calculations the surface tension coefficient of molten $Al_2O_3$ d□/dT = -6 $10^{-5}$ kg/s$^2$°C and the viscosity of μ = 0.105 kg/m s [24] has been used in the boundary condition (6). The same values has been applied for the simulation of the TiN-particle dispersing in SN80, since it can be assumed that the changes in these parameters due to the reinforcement of the alumina ceramic with 10 wt.% zirconia are small. The other relevant thermophysical parameters for alumina and the zirconia reinforced alumina and TiN are given in table I. The absorption efficiency η is set to 0.85 which has been evaluated by a comparison of temperature measurements and results of model calculations of the temperature distribution during the laser process [25].

For the solution of the equations described above, the PHOENICS-solver was used, which is based on the SIMPLE-algorithm (**s**emi-**i**mplicit **m**ethod for **p**ressure **l**inked **e**quations) [26]. The computational domain with dimensions of 8.0x1.9x1.0 mm$^3$ for the x-, y- and z-direction, respectively, were discretised using a mesh with 80x20x1 control volumes. These dimensions were chosen on the basis of repeated test calculations starting at the original geometry of the ceramic substrate and continuing with a stepwise reduction of the thickness and width of the domain in order to make sure that the heat affected zone is located completely within the domain, i.e. the boundary condition T=1500°C for the right, left and bottom boundary and the neighbouring cells was still valid. Symmetry boundary conditions were applied to the front and rear surface of the computational domain, which corresponds to an analysis of the geometry as a semi-infinite body. Within a mesh refinement study computations have been performed on meshes up to 160x40x1 control volumes. The refinement of the mesh did not affect the calculated results significantly, but gave a better spatial resolution of the solid liquid interface.

## 5 RESULTS AND DISCUSSION

The model geometry and typical numerical results calculated by the two dimensional FV-model for the case of the laser induced dispersing of TiN into the ceramic substrate are shown in fig. 2 and 3 for the one step and the two step process, respectively. Within this particular calculation a value of 300 W has been used for the laser power and 250 mm/min for the scanning velocity. Contour plots (Fig. 3) are shown for the fraction of liquid $F_{Liq}$ which characterises the extension of the melting pool for values $F_{Liq}<0.5$ and the position of the

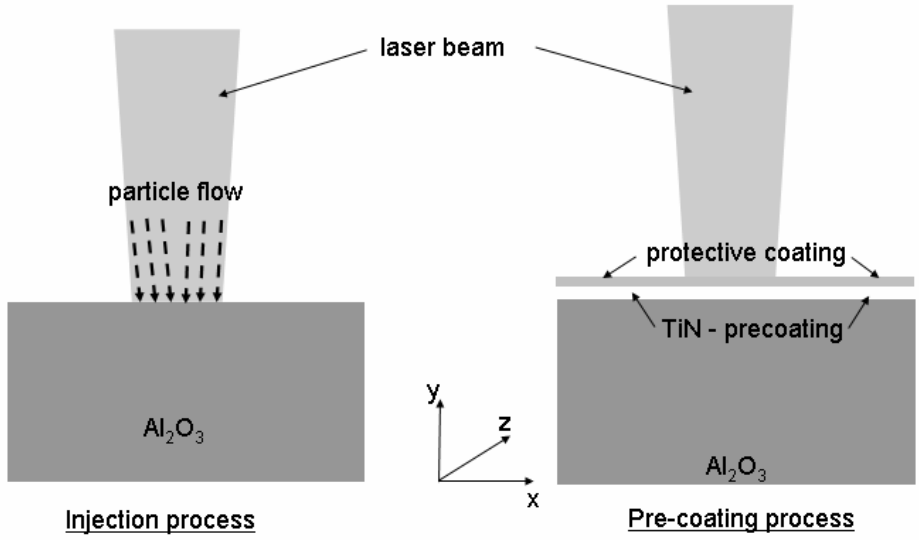


Figure 2: Schematics of the model geometry for the one step injection process (left) and two step pre-coating process (right)

liquid-solid phase boundary by $F_{Liq}$=0.5. The calculated distribution of the additive phase is shown by a contour plot of the model (Fig. 4) variable $C_{Part}$ which exhibits the volume fraction of the TiN phase.

The extension of the melting pool, and also the distribution of the additive material exhibits different characteristics, depending on process option used. In the case of the one-step process the shear forces at the surface of the melt pool induced by the finite temperature coefficient of the surface tension and the strong temperature gradient lead to a flat but wide melting pool. The second phase (TiN) is distributed homogenously only down to a certain dispersing depth which is lower than the maximum depth of the melting pool. In the two step process with the pre-coating and the protective overlayer the absence of shear forces lead to a slow sedimentation of the second phase into the molten region of the substrate. During the laser induced re-melting of the substrate and the overlayer the TiN pre-coating is infiltrated by molten alumina at early stages of the process and starts to sink into the molten pool later. After solidification the main part of metal-ceramic composite has been developed as a layer on top of the surface of the substrate in contrast to the one step process, where the second phase is incorporated completely.

In order to get more insight in the dominating process parameters further simulations has been performed with variation of the laser power density. Calculated melting and dispersing depth and the maximum volume fraction of the dispersed TiN phase in the Al24-substrate as a function of the power density divided by the laser scanning velocity, which corresponds to an

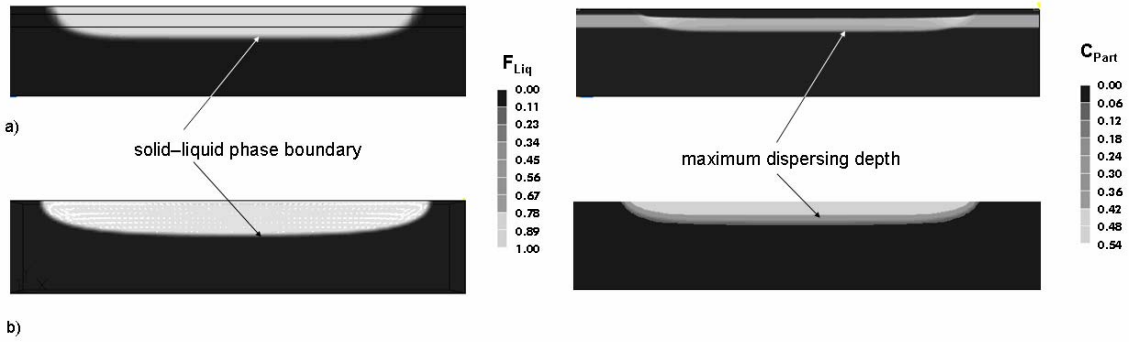


Figure 3: Contour plot of the fraction of liquid $F_{Liq}$ variable (right) representing the extension of the melt pool and volume fraction of the TiN particles $C_{Part}$ (left) showing the average distribution of the particles at the end of the process: a) pre-coating process- the black lines indicate the initial position of the powder coating-, b) injection process. A scanning speed of 250 mm/s and a laser power of 300 W have been used for the calculation.

energy over the travelling distance of the laser beam and can be taken as an effective energy along the laser line, are shown in fig. 4 for the processing with a TiN pre-coating. For the simulations a thickness value of 200 μm for TiN pre-coating and 100 μm for the $Al_2O_3$ over-layer has been used. From the diagram a critical power density level can be extracted where the behaviour of the melting/dispersing depth and also the TiN-volume fraction changes as a function of the laser power. For laser power values less than 300 W a metal-ceramic composite is generated on top the surface. At higher power levels the TiN pre-coating starts to sink into growing melt pool, leading to an increasing dilution of the particle volume fraction. This specific behaviour of has been identified in early studies of laser cladding with pre-placed powders[27] which has shown that at low power a surface composite is generated on the top of the substrate, whereas with increasing laser power the pre-placed powder layer is incorporated into the substrate. The latter effect leads to an increasing dilution with the growing volume of the melt pool. The results of the simulations have been confirmed by experimental data extracted from metallographic cross sections [28] of the processed samples, which are shown also in the diagram. Considering the experimental uncertainties these data are in good agreement with the numerical results.

The results of the simulation of the one-step injection process for the Al24-substrate are shown in fig. 4. As in the case for the pre-coating process the model calculations have been performed with varying laser power and scanning speed of the laser beam. The mass flux of the TiN particles was 270 mg/cm$^2$s. The overall level of the power density divided by the scanning speed is significantly lower than for the two step process since there is no the pre-coating layer which can act as a thermal barrier. The dispersing and melting depth varies smoothly as a function of the laser power density with this process option. The volume fraction increases also with higher laser power but reaches a saturation value of approximately 60 % at the highest level. This value is less than the maximum value of 64 % volume fraction

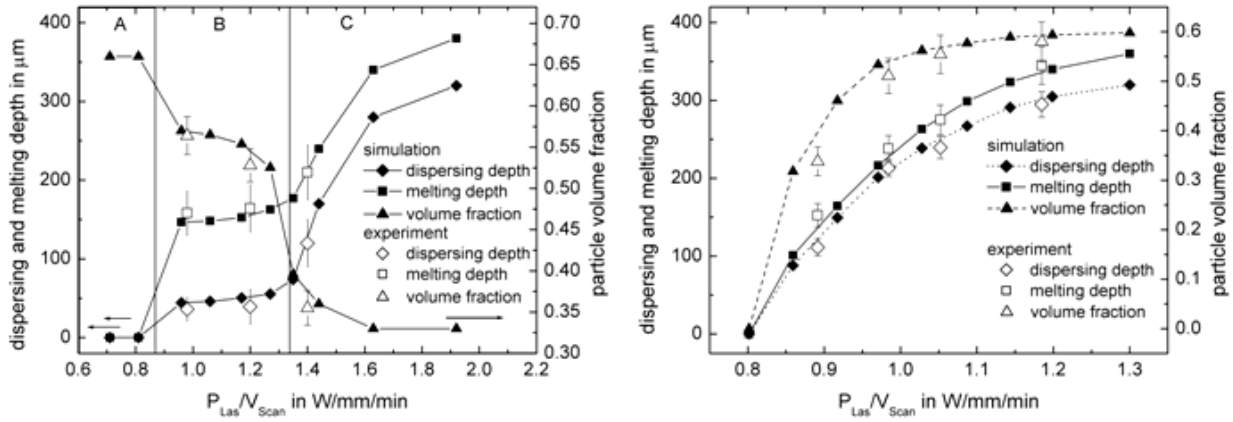


Figure 4: Calculated depth of dispersing and melting and maximum volume fraction of TiN particles in Al24 ($Al_2O_3$) as a function of the laser power divided by the scanning velocity for a laser process with a pre-placed powder coating (left) and with particle injection (right)

of a random close packing of spheres [29] which may be due the fact that the powder particles are mostly irregular shaped with a more or less pronounced deviation from perfect sphere. A critical power level, which separates a region, where a composite layer on top of the surface develops, from a power regime, which is characterised by the settling of the metal particles below the original surface of the substrate, can not be observed as in the case of the pre-coating process applied to the Al24-substrate. Also for this process option the comparison with the experimental data confirm the good agreement of the measured data with the results of the simulation.

The different behaviour of the particle volume fraction as a function of the laser power and scanning speed using the particle injection or the pre-coating option of the process can be explained by the difference in the available total mass of the powder particles: For the pre-coating option the total powder mass or volume delivered by the pre-placed coating is a constant. Therefore increasing dilution effects occur if it is distributed over a growing volume of the melt pool. For the injection option the mass flow through the feeding nozzle is a constant which leads to an increasing accumulated mass within the melt pool with decreasing scanning speed.

The simulations has been extended to the $ZrO_2$ reinforced alumina SN80 in order to compare the laser dispersing process of hard metal particles in an isothermal melting and solidifying ceramics like the Al24-substrate with the binary system SN80 which solidifies over a wide temperature range [30, 31]. While the Al24 ceramics solidifies at a temperature of 2040 °C and the SN80 has a liquidus temperature of 2020 °C and a solidus temperature of 1890 °C, it can be expected that both systems behave different during the laser modification process. The results of the simulations for TiN dispersed in SN80, using the pre-coating

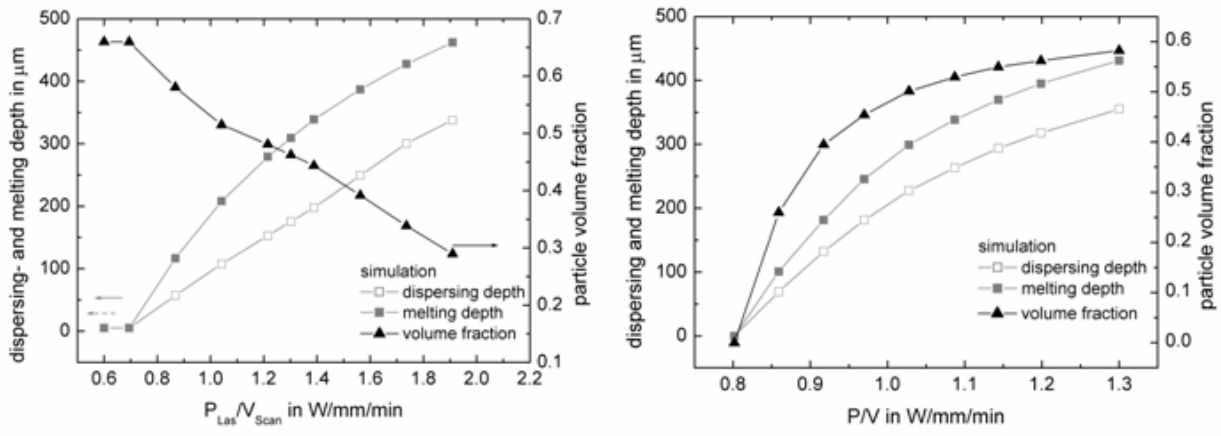


Figure 5: Results of the simulation for laser dispersed TiN-particles in SN80 ($90Al_2O_3$-$10ZrO_2$) as a function of the laser power divided by the scanning velocity for a process with a pre-placed powder coating (left) and with particle injection (right)

process option, are shown in fig. 5. The melting and dispersing depth increases continuously as a function of the laser power over the scanning velocity without any significant change in its slope. Consequently, the volume fraction of the TiN-particles decreases with the rising energy input, leading to a continuous dilution of the second phase within the growing melt pool. The calculations for the laser induced TiN-particle dispersing in SN80 using the injection process option has been performed with the same process parameters as for the Al24 substrate. The simulation results are shown in fig. 8, which shows continuously increasing values of the melting and dispersing depth as well as the particle volume fraction as a function of the laser power divided by the scanning velocity.

## 6 SUMMARY AND CONCLUSION

A numerical model has been presented for the simulation of laser induced surface modification processes of ceramics. Two process options have been considered in the model for the transfer of a second phase material into the ceramic substrate: A pre-coating process which utilises a metallic layer applied prior to the laser-solid interaction and an injection process in which a powder flow is directed onto the ceramic surface during the laser induced re-melting. For the injection process the mass transport within the molten ceramic pool is driven by the temperature coefficient of the surface tension and the temperature gradient at the liquid-gas interface. In the pre-coating process the slow sedimentation of the second phase leads to a distribution of metal particles which shows characteristic features in the isothermal melting ceramics Al24 depending on the effective laser energy input in a critical way.

Applying this process option to the binary system SN80 this critical behaviour can not be observed, since the melting and dispersing depth and also the particle volume fraction are changing continuously with varying process parameters. Using the one step injection process both substrate systems behave very similar over the considered range of process parameters with only small differences in the melting and dispersing depth.

From the numerical results it can be concluded that the binary system SN80 with its lower melting temperature, which is closer to the pre-heating temperature, and its wider solidification range has some advantages for the laser processing compared to the isothermal melting pure alumina.

## 7 ACKNOWLEDGEMENTS

These studies were supported by the Deutsche Forschungsgemeinschaft (DFG) in context with the Sonderforschungsbereich 483 “High performance sliding and friction systems based on advanced ceramics”.

## REFERENCES

[1] K.-H. Zum Gahr and J. Schneider, “Surface Modification of Ceramics for Improved Tribological Properties”, Ceram. Int., **26**, 363-370 (2000)

[2] S. Rüdiger, H. Gruhn H., R. Heidinger, M. Rohde, J. Schneider, and K.-H. Zum Gahr, “Laser induced surface modification of cordierite”, in *Surface Engineering* EUROMAT 99, H. Dimigen (ed.), **11**, 510 – 515 (1999)

[3] U. Duitsch, S. Schreck and M. Rohde, “Experimental and numerical investigation of heat and mass transport in laser-induced modification of ceramic substrates”, Int. J. Thermophys., **24**, 731-740 (2003)

[4] A. Kar and J. Mazumder, “One Dimensional Model for Extended Solid Solution in Laser Cladding”, J. Appl. Phys., **61**(7), 2645-2655 (1987)

[5] M. Picasso and A.F.A. Hoadley, “Finite Element Simulation of Laser Surface Treatments Including Convection in Melt Pool”, Int.J. Meth. Heat Fluid Flow, **4**, 61-83 (1994)

[6] X. He, B.L. Mordike, N. Pirch, E.W. Kreutz: “Laser surface alloying of metallic materials”, Laser Eng. **4**, 291-316 (1995)

[7] Bamberger, W.D. Kaplan, B. Medres, L. Shepeleva, “Calculation of process parameters for laser alloying and cladding”, J. Laser Appl. **10**, no. 1, 29-33 (1998)

[8] S. Sakar, P. Mohan Raj, S. Chakraborty, G. Phanikumar, K. Chattopadhyay, and P. Dutta, “Transport phenomena in laser surface alloying”, J. Mat. Sci., **38**, 155-164 (2003)

[9] E. Toyserkani, A. Khajepour, and S. Corbin, “3-D finite element modelling of laser cladding by powder injection: effects of pulse shaping on the process”, Optics & Lasers Eng., **41,** 849-867 (2004)

[10] S.Z. Shuja, B.S. Yilbas and M.O. Budair, “Modelling of laser heating of solid substance including assisting gas impingement”, Numerical Heat Transfer., part A, **33**, 315-339,

(1998)
[11] S. Sakar, P. Mohan Raj and S. Chakraborty, "3D-Computational modeling of momentum, heat and mass transfer in a laser alloying process", Numerical Heat Transfer, part A, **42**, 307-326 (2002)
[12] I. H. Chowdhury and X. Xu, "Heat transfer in femtosecond laser processing of metal, Numerical Heat Transfer", Part A, **44**, 219-232 (2004)
[13] S. Roychoudary and T. L. Bergman, "Response of agglomerated, multiceramic particles to intense heating and cooling for thermal plasma spraying simulation", Numerical Heat Transfer, Part A, **46,** 211-233 (2004)
[14] I. Ahmed, and T.L. Bergman, "An engineering model for solid-liquid phase change within sprayed ceramic coatings of nonuniform thickness", Numerical Heat Transfer, Part A, **41**, pp. 113-129 (2002)
[15] J.F. Li, L.Li, and F.H. Stott, "Predictions of Flow Velocity and Velocity Boundary Layer Thickness at Surface During Laser Melting of Ceramics", J. Phys.D Appl. Phys., **33**, 945-947 (2004)
[16] J. Cheng and A.Kar, "Mathematical Model for Laser Densification of Ceramic Coating", J. Mater. Sci., **32**, 6268-6278 (1997)
[17] D.B. Spalding: PH*OENICS Overview, Cham Technical Report: TR 001* (CHAM, UK, 2001)
[18] M. Rohde, "Thermophysical properties of ceramic substrates with modified surfaces", submitted to Int. J. Thermophys.
[19] M. Rohde and B. Schulz, "Radiation Damage in Fusion Window Materials Studied by Thermal Conductivity", ASTM, Special Technical Publication 1125, R.E. Stoller, A.S. Kumar and D.S. Gelles (eds.), pp. 764-775, (1992)
[20] J. Bousinesq, *Theorie Analytique de la Chaleur*, Gauthier-Villars, (1903)
[21] A.D. Brent, V.R. Voller, and J. Reid, "The Enthalpy Porosity Technique for Modelling Convection-Diffusion Phase Change: Application to the Melting of a Pure Metal", Numerical Heat Transfer, **13**, pp. 297-318, (1988)
[22] V.R. Voller and C. Prakash, "A fixed grid numerical modelling methodology for convection-diffusion mushy region phase change problems", Int. J. Heat. Mass Transfer, **30**, 1709-1721, (1987)
[23. R. Clift, J.R. Grace and M.E. Weber, *Bubbles, Drops and Particles*, Academic Press, New York, (1978)
[24] B. Glorieux, F. Millot and J.C. Rifflet: "Surface tension of liquid alumina from contactless techniques", Int. J. Thermphys., **23** (5), 1249-1257 (2002)
[25] H. Gruhn, R. Heidinger, M. Rohde, S. Rüdiger, J. Schneider and K.-H. Zum Gahr, "Laser Induced Surface Modification of Ceramic Substrates for Thermal and Electrical Lines in Microsystems: Modeling Compared to Experiment", MSM 99, Int. Conf. modeling and Simulation of Microsystems, pp. 105-108 (1999)
[26] S.V. Patankar and D.B. Spalding, "A Calculation Procedure of Heat, Mass and Momentum Transfer in Three Dimensional Parabolic Flows", Int. J. Heat Mass Transfer, **15,** 1787- 1799 (1972)
[27] J. Powell, P.S. Henry, and W.M. Steen, "Laser Cladding with Preplaced Powder:

Analysis of Thermal Cycling and Dilution Effects", Surf. Eng., **4** (2), 141-149 (1988)
[28] K. Poser, J. Schneider, M. Rohde, and K.-H. Zum Gahr, "Tin-particle reinforced alumina for unlubricated tribological applications mated with metallic counterbodies", Mat.-wiss. u. Werkstofftechn., **36**, 122-128 (2005)
[29] H.M. Jaeger and S.R. Nagel, "Physics of the Granular State", Science, **255**, 1523-131 (1992)
[30] T.B. Massalski, *Binary alloy phase diagrams,* Vol. 3, ASM International, (1990)
[31] S. Bourban, N. Karapatis, H. Hofmann, and W. Kurz, "Solidification microstructures of laser remelted $Al_2O_3$-$ZrO_2$ eutectic", Acta Mater., **45** (12), 5069-5075 (1997)
[32] Y.S. Touloukian, *Thermophysical properties of matter*, Vol. 3, Plenum Press, N.Y. (1970)